

**Figure 4** The dependence of gain characteristics on the lasing signal power at 1540 and 1560 nm

ever, when the lasing signal powers are higher than 2.5 dBm, the gain saturation at L band takes place, and hence the gain is reduced. This behavior is attributed to the low saturation power at L band. In order to obtain the high gain for a given EDF length, the optimal attenuation in the ring cavity is required to achieve the optimum lasing power.

#### 4. CONCLUSION

Improvement of L-band signal gain by employing the lasing wavelengths as the secondary pump source for the EDF has been demonstrated. A spontaneous emission spectrum up to a wavelength of 1635 nm is observed. The experimental results show that the gain depends on the absorption coefficient of the C band. This indicates the efficiency of the energy transfer between these two bands. The lasing signal powers and the lasing wavelengths also influence the L-band gain. This is ascribed to the interplay between the absorption and amplification of EDF. The experiments imply that the suggested EDFA configuration is applicable to any pump wavelength, because deploying 1480-nm pump laser diodes can provide better power conversion efficiency and generate stronger C-band lasing. Therefore, it is believed that this approach will play an important role in the development of L-band EDFAs for practical DWDM communication systems.

#### REFERENCES

1. M. Yamada, H. Ono, T. Kanamori, S. Sudo, and Y. Ohishi, Broad-band and gain-flattened amplifier composed of a 1.55  $\mu\text{m}$ -band and a 1.58  $\mu\text{m}$ -band  $\text{Er}^{3+}$ -doped fiber amplifier in a parallel configuration, *Electron Lett*, 33 (1997), 710–711.
2. H. Ono, M. Yamada, T. Kanamori, S. Sudo, and Y. Ohishi, 1.58- $\mu\text{m}$  band gain-flattened erbium-doped fiber amplifiers for WDM transmission systems, *J Lightwave Technol*, 17 (1999), 490–496.
3. J.F. Massicot, R. Wyatt, and B.J. Ainslie, Low noise operation of  $\text{Er}^{3+}$ -doped silica fiber amplifier around 1.6  $\mu\text{m}$ , *Electron Lett*, 28 (1992), 1924–1925.
4. J.H. Lee, U.C. Ryu, S.J. Ahn, and N. Park, Enhancement of power conversion efficiency for an L-band EDFA with a secondary pumping effect in the unpumped EDF section, *IEEE Photon Technol Lett*, 11 (1999), 42–44.
5. J. Nilsson, S.Y. Yun, S.T. Hwang, J.M. Kim, and S.J. Kim, Long-wavelength erbium-doped fiber amplifier gain enhanced by ASE end-reflectors, *IEEE Photon Technol Lett*, 10 (1998), 1551–1553.

## DETECTION OF TARGETS IN CONTINUOUS RANDOM MEDIA: A NUMERICAL STUDY USING THE ANGULAR CORRELATION FUNCTION

C. D. Moss,<sup>1</sup> F. L. Teixeira,<sup>2</sup> and J. A. Kong<sup>1</sup>

<sup>1</sup> Research Laboratory of Electronics  
Massachusetts Institute of Technology  
Cambridge, Massachusetts 02139

<sup>2</sup> ElectroScience Laboratory and Department of Electrical Engineering  
The Ohio State University  
Columbus, Ohio 43210

Received 13 November 2001

**ABSTRACT:** A three-dimensional (3D) finite-difference–time-domain (FDTD) scheme is used to study the angular correlation function (ACF) of the scattered fields from continuous random media (volume) with and without a target object present. The FDTD simulations are employed to examine the effectiveness of ACF for object detection in the presence of volumetric clutter. It is shown that the frequency-averaged ACF can be as much as 10-dB greater when a target object is present for situations where the target is undetectable by direct examination of the radar cross section only. © 2002 Wiley Periodicals, Inc. *Microwave Opt Technol Lett* 33: 242–247, 2002; Published online in Wiley InterScience (www.interscience.wiley.com). DOI 10.1002/mop.10287

**Key words:** target detection; 3D FDTD; random media; numerical methods

#### 1. INTRODUCTION

Electromagnetic-wave propagation in random media is a topic of great importance in fields such as remote sensing [1] and communications [2]. This is because many natural media such as foliage or soil cannot be described in a purely deterministic manner. For example, predictions of radar return from objects obscured by foliage or buried under the soil are clearly dependent on the knowledge of the effects of such media on the total scattered field response (clutter).

Random media have constitutive parameters that are random variables in space (or time). Statistical models can be used to characterize a random medium in terms of an effective (mean) permittivity (or permeability), and fluctuations described by some correlation function. The study of statistical properties of electromagnetic wave scattering in such media can be carried out by Monte Carlo simulations on an ensemble of random media. In some very particular cases, a single realization may be sufficient by assuming spatial ergodicity, but in general, the Monte Carlo ensemble should be large enough to ensure statistically meaningful results. The statistical description of random volumetric material inhomogeneities in this way is similar to the statistical description of random rough surfaces [3].

This work will characterize soil as an inhomogeneous, continuous random media with subsurface detection applications in mind [4–8]. A number of studies have demonstrated that the soil constitutive parameters are highly sensitive to both moisture [9] and material content [10], so it is important to characterize such effects in terms of random permittivity fluctuations.

The bistatic scattered fields from targets buried in random media have recently been studied with both ensemble and frequency-averaging techniques [11]. Here 3D FDTD simulations [12] will be used to characterize the angular correlation function (ACF) of the scattered fields of targets in continuous random media. This result will serve to verify the effectiveness of the ACF

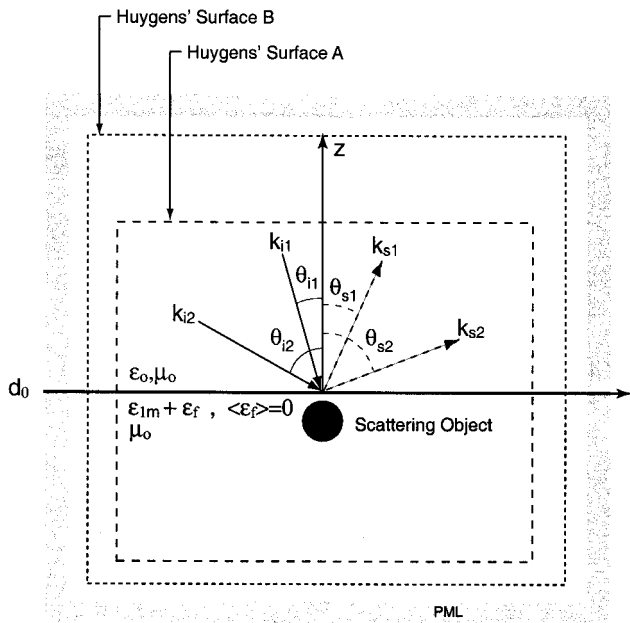


**Figure 1** Object is a cylinder, buried in the random medium half space;  $\epsilon_{1m} = 3.5$

for object detection in situations where the clutter from the surrounding volumetric scattering is important. The ACFs generated from FDTD simulations are also compared against ACFs obtained from the Born approximation (when the latter is applicable) and excellent agreement is obtained.

## 2. FDTD AND RANDOM MEDIUM MODELS

Our FDTD computational domain is shown in Figure 1, containing a perfect electrically conducting (PEC) cylinder embedded in a random medium half space. The incident field is introduced on the Huygens' surface A enclosing the target as well as the random-medium half space, with the use of the total/scattered (T/S) field formulation [12]. With the use of plane-wave incidence, the half-space Green's function [5] is used to calculate the incident field everywhere on the Huygens' surface A. The half-space Green's function is carefully adjusted to incorporate the numerical dispersion effects, thus minimizing numerical noise in the scattered field region [13]. When calculating the incident field, the permittivity of the half space is taken to be the effective permittivity of the random medium. The scattered far field is calculated on the Huygens' surface B in the scattered field domain [14], again with the use of the layered Green's function. A perfectly matched layer (PML) formulated via stretched coordinates [15] is used to match the interior medium and truncate the computational domain.

The results presented here do not include the direct reflection from the half-space interface (free-space/mean permittivity). The interface return (surface scattering) is removed because the interest lies in the perturbations to the RCS response caused by the buried object and the random medium. Therefore, the scattered field results shown can be considered as perturbations in the steady-state average return with no object present. If necessary, direct returns from the interface layer can be easily obtained (even analytically). Moreover, because we assume a planar interface, the simulations presented here do not include any surface roughness (and the associated surface-scattering clutter) effects in the scattering results. This is purposely done in order to isolate and better analyze the volumetric scattering effects.

The random media correlation lengths are considered to be on the order of a wavelength, so that the fluctuations are directly mapped into the FDTD domain. The permittivity is characterized as

$$\epsilon(\vec{r}) = \epsilon_m + \epsilon_f(\vec{r}), \quad (1)$$

where  $\vec{r} = x\hat{x} + y\hat{y} + z\hat{z}$  and  $\epsilon_f(\vec{r})$  is a function of position  $\vec{r}$  characterizing the random fluctuation, and is such that  $\langle \epsilon_f(\vec{r}) \rangle = 0$ . The fluctuation at each position is a Gaussian random variable, with correlation function  $C(\vec{r}_1 - \vec{r}_2)$ . The generation of  $\epsilon_f(\vec{r})$  is implemented in the Fourier domain by passing a three-dimensional array of random numbers (with Gaussian distribution and zero mean) through a digital filter whose response corresponds to  $W(\vec{k})$ , the Fourier transform of  $C(\vec{r}_1 - \vec{r}_2)$ .  $W(\vec{k})$  is then the spectral density function of the dielectric fluctuation. The following correlation function is used:

$$\begin{aligned} \langle \epsilon_f(\vec{r}_1) \epsilon_f^*(\vec{r}_2) \rangle &= C(\vec{r}_1 - \vec{r}_2) \\ &= \delta \epsilon_{1m}^2 \exp\left(-\frac{(|x_1 - x_2|^2 + |y_1 - y_2|^2)}{l_p^2}\right) \exp\left(-\frac{|z_1 - z_2|^2}{l_z^2}\right), \quad (2) \end{aligned}$$

where  $l_p$  and  $l_z$  are the transverse and vertical correlation lengths, respectively,  $\epsilon_{1m}$  is the mean permittivity, and  $\delta$  is the variance. The correlation function in Eq. (2) has a Gaussian profile in both the transverse and vertical directions [16,17]. A typical  $x - y$  plane cross section of one realization is depicted in Figure 2. Note that other correlation functions could be used as well. A Gaussian correlation is used here for its generality and because it can be fully described with a minimal number of parameters  $l_p$ ,  $l_z$ ,  $\epsilon_{1m}$ , and  $\delta$  (low-order statistics).

## 3. ANGULAR CORRELATION FUNCTION (ACF)

The ACF [18] is the correlation between two scattered waves in directions  $\theta_{s1}$  and  $\theta_{s2}$ , resulting from two incident waves in directions  $\theta_{i1}$  and  $\theta_{i2}$ . Generally, the angles can be a function of  $\phi$  or  $\theta$  in a three-dimensional geometry such as the one under consideration, but for now we limit  $\phi_{i1} = \phi_{i2} = 0$ . The ACF,  $\Gamma$ , is written as

$$\Gamma(\theta_{s1}, \theta_{i1}; \theta_{s2}, \theta_{i2}) = \langle E_s(\theta_{s1}, \theta_{i1}) E_s^*(\theta_{s2}, \theta_{i2}) \rangle, \quad (3)$$

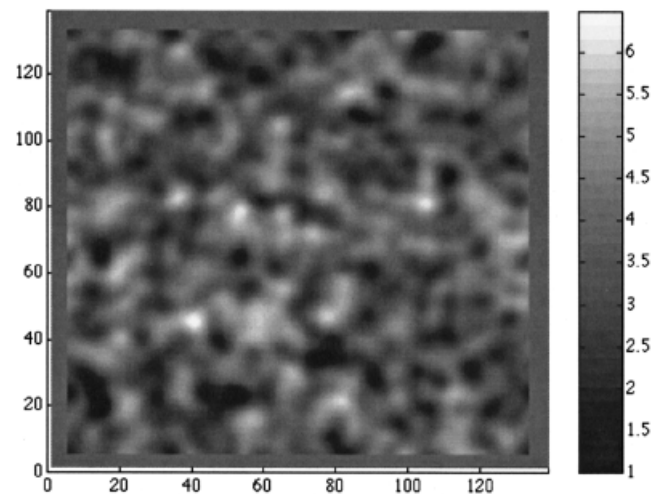


**Figure 2** Cross-section of the random-medium permittivity in the  $x$ - $y$  plane.  $\epsilon_{1m} = 3.5$

where  $E_s$  is the scattered field and the angular brackets denote averaging. The averaging can be performed in many ways, the most common being realization averaging:

$$\Gamma_r(\theta_{s1}, \theta_{i1}; \theta_{s2}, \theta_{i2}) = \frac{1}{N_r} \sum_{n=1}^{N_r} \psi_s^N(\theta_{s1}, \theta_{i1}, n) \times \psi_s^{N*}(\theta_{s2}, \theta_{i2}, n) / \sqrt{P_1 P_2}, \quad (4)$$

and frequency averaging [19]:

$$\Gamma_f(\theta_{s1}, \theta_{i1}; \theta_{s2}, \theta_{i2}) = \frac{1}{N_f} \sum_{n=1}^{N_f} \psi_s^N(\theta_{s1}, \theta_{i1}, f_n) \times \psi_s^{N*}(\theta_{s2}, \theta_{i2}, f_n) / \sqrt{P_1 P_2}, \quad (5)$$

where the bandwidth can be defined as  $2 \Delta f, f_o - \Delta f < f_n < f_o + \Delta f$ ,  $N_r$  and  $N_f$  are the number of medium realizations and frequencies, respectively, and  $P_1, P_2$  describe the power of the incident fields. Equation (3) has a correlation that is described by what is known as the memory effect, which is a function of the incident and scattered wave angles. The memory effect is a result of the *statistical* translational invariance of the random volume, and reduces to phase matching for the deterministic (zero variance) case. In the case of a random rough *surface* scattering, the strongest correlation occurs along the *memory line*, described by  $\sin \theta_{s2} - \sin \theta_{s1} = \sin \theta_{i2} - \sin \theta_{i1}$ . When considering *volumetric* scattering from a random medium, another phase-matching condition exists in the vertical direction, described by  $\cos \theta_{i1} + \cos \theta_{s1} = \cos \theta_{i2} + \cos \theta_{s2}$ . This latter phase-matching condition makes the memory line shorter [19], creating what is called a *memory dot*. Note that random medium scattering is not statistically invariant in the vertical direction, because of loss (finite conductivity), so this memory effect is not exact.

Realization averaging is akin to Monte Carlo averaging, and is very useful to describe the statistical properties of scattered fields. However, although realization averaging is useful in demonstrating the memory effects theoretically, it cannot be applied to real subsurface detection problems because only one realization is available in practice.

Frequency averaging is an alternative technique that can be used in practical detection problems. FDTD is suited for simulations involving frequency averaging, with proper care taken to avoid numerical dispersion effects at higher frequencies. Moreover, the objects must be relatively shallow, because of the frequency dependence of penetration depth. A weighting function  $W_e(f)$  must then be used to compensate for the frequency-dependent response of the system (penetration depth, object size) [19]. This work will examine both realization and frequency averaging techniques.

The motivation for using the ACF is that scattered fields from buried objects should exhibit greater correlation than the random medium clutter, especially away from the memory line (or dot). This is particularly true when the object has some kind of symmetry (such as spherical or cylindrical). The goal then is to compare the ACF of a random medium for cases with and without an buried object present, with the hope that the ACF will exhibit significant differences.

#### 4. BORN APPROXIMATION

This section describes the Born approximation used to validate the FDTD results for half-space problems with low contrast. Given a

plane wave incident on the half-space random medium defined in Section 2, the fields in regions 0 (upper) and 1 (lower) can be calculated with the use of the dyadic layered Green's functions,  $\bar{G}_{01}^{(0)}(\bar{r}, \bar{r}')$  and  $\bar{G}_{11}^{(0)}(\bar{r}, \bar{r}')$ , as [20]

$$\bar{E} = \bar{E}^{(0)} + \omega^2 \mu \int_{V_1} d\bar{r}' \bar{G}_{01}^{(0)}(\bar{r}, \bar{r}') \varepsilon_{1f}(\bar{r}') \cdot \bar{E}_1(\bar{r}'), \quad (6)$$

$$\bar{E}_1 = \bar{E}_1^{(0)} + \omega^2 \mu \int_{V_1} d\bar{r}' \bar{G}_{11}^{(0)}(\bar{r}, \bar{r}') \varepsilon_{1f}(\bar{r}') \cdot \bar{E}_1(\bar{r}'), \quad (7)$$

where  $V_1$  is the random medium volume. With the Born approximation [20] used to obtain the first-order solution, the total field  $\bar{E}_1$  in the integral is replaced by the incident field  $\bar{E}_1^{(0)}$ . The approximation is applicable when  $\varepsilon_{1f}(\bar{r}') \approx \varepsilon_{1m}$  (low contrast).

The perturbed part of the scattered field in region 0 is then

$$\bar{E}_s^{(1)}(\bar{r}) = \omega^2 \mu \int_{V_1} d\bar{r}' \bar{G}_{01}^{(0)}(\bar{r}, \bar{r}') \varepsilon_{1f}(\bar{r}') \cdot \bar{E}_1^{(0)}(\bar{r}'). \quad (8)$$

The half-space Green's function in the far field is

$$\bar{G}_{01}^{(0)}(\bar{r}, \bar{r}') = \frac{e^{ikr}}{4\pi r} \left[ X_{01s} \hat{h}(\theta_s, \phi_s) \hat{h}(\theta_{s1}, \phi_{s1}) + \frac{k}{k_{1m}} Y_{01s} \hat{v}(\theta_s, \phi_s) \hat{v}(\theta_{s1}, \phi_{s1}) \right] e^{-i\bar{k}_s \bar{r}'}, \quad (9)$$

where  $X_{01s}$  and  $Y_{01s}$  are the transmission coefficients of the half-space interface, with the subscript  $s$  indicating they are evaluated in the direction of the scattered fields, and  $\hat{h}$  and  $\hat{v}$  are the standard polarization vectors [20]. Given two incident fields in region 0,  $\bar{E}_{ia}$  and  $\bar{E}_{ib}$ , the unperturbed fields in region 1 are obtained as

$$\bar{E}_{1a}^{(0)}(\bar{r}) = X_{01a} \hat{h}_{1a} e^{i\bar{k}_{1a} \bar{r}}, \quad (10)$$

$$\bar{E}_{1b}^{(0)}(\bar{r}) = X_{01b} \hat{h}_{1b} e^{i\bar{k}_{1b} \bar{r}}, \quad (11)$$

where the transmission coefficients, polarization vectors, and  $k$  vectors are denoted with  $a$  or  $b$  subscripts to correspond to the respective incident fields.

The co-polarized ACF using ensemble averaging and the Born approximation can then be written as

$$\Gamma_{ab} = \frac{k_m^4 \delta}{16\pi^2 r^2} X_{01sb} X_{01ib} X_{01sa} X_{01ia} A, \quad (12)$$

where  $A$  is

$$A = \int_{V_1} d\bar{r}' \int_{V_1} d\bar{r}'' e^{i(\bar{k}_{1a} \bar{r}' - \bar{k}_{1b} \bar{r}'')} C(\bar{r}' - \bar{r}'') \quad (13)$$

and  $k_{d1a}$  is  $k_{1ia} - k_{1sa}$  (similarly for  $k_{d1b}$ ). Changing to average and difference coordinates,  $\hat{r}_{av} = (\hat{r}' + \hat{r}'')/2$  and  $\hat{r}_d = \hat{r}' - \hat{r}''$ , leads to

$$A = \int_{V_1} d\bar{r}_{av} \int_{V_1} d\bar{r}_d \exp[i((\bar{k}_{d1a} - \bar{k}_{d1b}) \cdot \bar{r}_a + (\bar{k}_{d1a} + \bar{k}_{d1b}) \cdot \bar{r}_d/2)] C(\bar{r}_d). \quad (14)$$

Evaluating the  $A$  factor results in

$$A = \frac{4i(e^{-ik_{z1d}^d} - 1)}{k_{z1d}^d} \frac{\sin k_{x1d}^d L_x/2}{k_{x1d}^d} \frac{\sin k_{y1d}^d L_y/2}{k_{y1d}^d} \frac{\pi^{3/2} l_p^2 l_z}{4} \times \exp\left[-\frac{l_p^2}{16}(k_{x1d}^d + k_{y1d}^d) - \frac{l_z^2}{16} k_{z1d}^d\right] \left[ \operatorname{erf}\left(\frac{L_x}{l_p} + \frac{ik_{x1d}^d l_p}{4}\right) + \operatorname{erf}\left(\frac{L_x}{l_p} - \frac{ik_{x1d}^d l_p}{4}\right) \right] \left[ \operatorname{erf}\left(\frac{L_y}{l_p} + \frac{ik_{y1d}^d l_p}{4}\right) + \operatorname{erf}\left(\frac{L_y}{l_p} - \frac{ik_{y1d}^d l_p}{4}\right) \right] \times \left[ \operatorname{erf}\left(\frac{d}{l_z} + \frac{ik_{z1d}^d l_z}{4}\right) + \operatorname{erf}\left(\frac{d}{l_z} - \frac{ik_{z1d}^d l_z}{4}\right) \right], \quad (15)$$

where  $k_{x1d}^d = k_{x1da} - k_{x1db}$  and  $k_{x1d}^d = k_{x1da} + k_{x1db}$ .

The dominant factors in the ACF are the first three factors of  $A$ , which are sinc functions in terms of  $k_x$ ,  $k_y$ , and  $k_z$ . These results show that the width of the memory line (or dot) is on the order of  $\lambda/L_x$  and  $\lambda/L_y$ , where  $L_x$  and  $L_y$  are the transverse linear dimensions of the random medium volume considered (illuminated area). The depth of the random medium is indicated by  $d$ ; hence the random permittivity fluctuations exist over a total volume defined by  $L_x \times L_y \times d$  in the half space. As shown in [11], larger correlation lengths result in larger scattered fields, and hence the total ACF increases in magnitude as the correlation lengths increase (the shape remains similar). However, as the correlation length approaches the dimensions of the volume, the ACF rapidly decreases to zero, as the random medium becomes homogeneous. The ACF is determined by averaging over angles to obtain different wave vectors. However it is also possible to obtain the frequency correlation function (FCF) by averaging over frequency (the sinc functions depend only on  $k$ ), although it is not as likely that the scattered fields of the object will be as well correlated over frequency as they are over angles. Hence, it is not expected that the FCF will have a significantly greater correlation when the object is placed in the random medium.

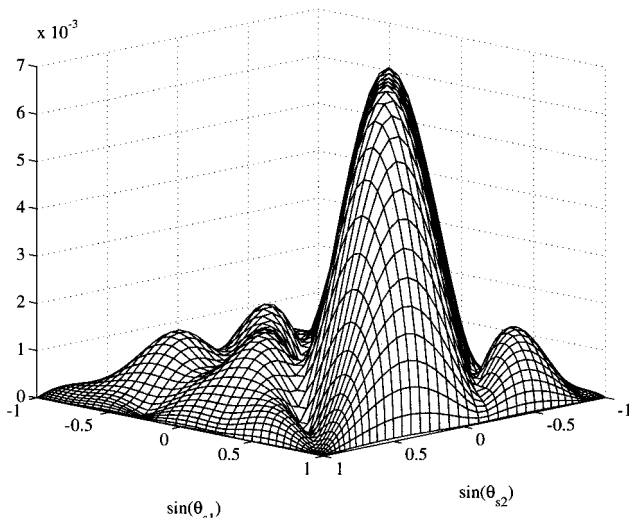


**Figure 3** ACF magnitude for the random medium without an object, using random medium averaging

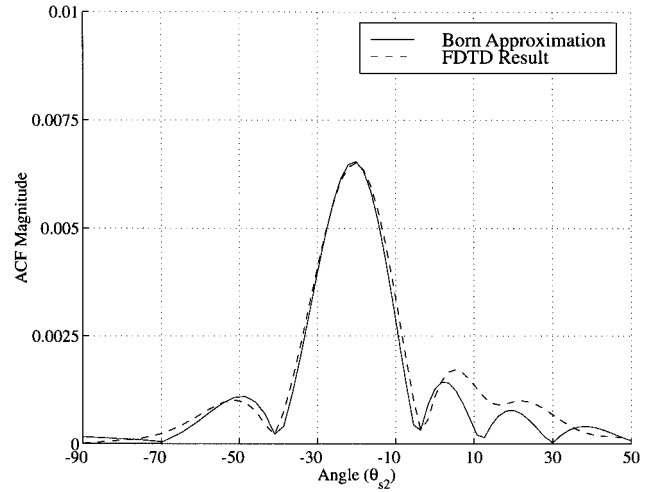


**Figure 4** Comparisons of the ACF obtained from FDTD and the Born approximation, plotted perpendicular to the memory line

## 5. RESULTS

The FDTD computational domain is created by discretizing the half space into a  $140 \times 140 \times 74$  lattice (composed of the standard Yee cells [21]), where the random soil comprises  $128 \times 128 \times 64$  cells. This results in a system with 12.85 million unknowns, solved at 1000 time steps, taking 683 seconds per realization on an AlphaServer DS20E (667 MHz with 4 GB RAM). The actual physical size of the random medium corresponds to  $1.71 \text{ m} \times 1.71 \text{ m} \times 0.855 \text{ m}$ . The discretization size is chosen to be 1.2 cm, which corresponds to  $\lambda/84$  in free space and approximately  $\lambda/45$  within the soil (mean permittivity) for a 300-MHz pulse (center frequency). In terms of the central frequency and the corresponding soil wavelength, the electrical size of the random medium is  $3.2\lambda \times 3.2\lambda \times 1.9\lambda$ .

The soil model has an average relative permittivity of  $\epsilon_{1,m} = 3.5$  and conductivity  $\sigma = 3.37 \times 10^{-3}$  [S/m], which have been experimentally determined [22] for a Puerto Rico type of clay loam [23]. The standard deviation of the soil permittivity is chosen to be between 15% and 25% of the mean value. These values roughly correspond to moisture content (water volume) fluctuations of a few percent, with a mean moisture content approximately 5%. The random medium has correlation lengths ( $l_p$  and  $l_z$ ) corresponding to approximately 5–7 FDTD cells (0.4 m).

First the FDTD results are compared to the Born approximation. The incident field angles are  $\theta_{s1} = 20^\circ$ ,  $\theta_{s2} = -10^\circ$ . Figure 3 shows the FDTD simulated ACF magnitude with no object versus the scattered field angle, averaged over 75 realizations. The strong correlation along the memory line, described by  $\sin \theta_{s2} - \sin \theta_{s1} = -0.515$ , is clearly visible. A peak occurs at the intersection with the vertical phase matching condition  $\cos \theta_{s2} - \cos \theta_{s1} = -0.0451$ . The correlation away from the memory line is relatively weak. Figure 4 shows the comparison of the ACF obtained with both the FDTD results and the Born approximation. The agreement is generally good, especially at the memory line. Generally, the Born approximation results overestimate the scattered fields, although it is not noticeable given these parameters. In this figure, the agreement is poorest away from the memory line, although this is not always the case.

To study the effectiveness of the ACF for object detection, a PEC cylinder (discretized with the use of a conformal FDTD [12]) is placed inside the random medium. The cylinder is approximately 10 cm in length and 9 cm in diameter, and it is buried 7 cm

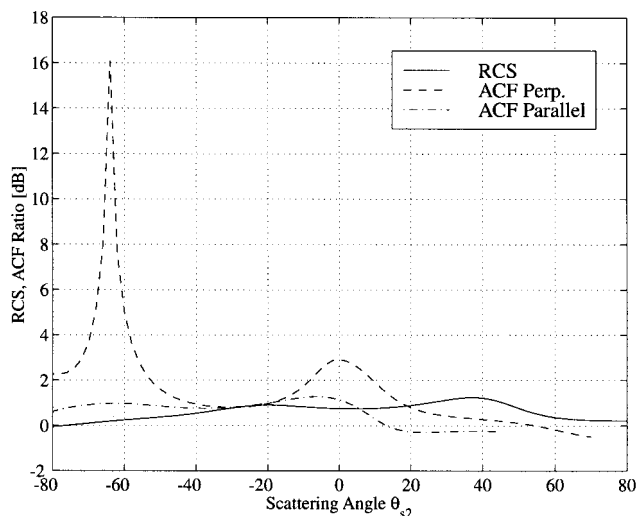


**Figure 5** Frequency-averaged RCS and ACF results, along and perpendicular to the memory line. The domain is  $3.2\lambda \times 3.2\lambda \times 1.6\lambda$

below the surface. The ACF and bistatic RCS of the scattered fields can then be compared (in dB), with and without the target present, with the use of

$$\Lambda_{ACF} = \frac{|\Gamma_f(\text{object})|}{|\Gamma_f(\text{no object})|}, \quad (16)$$

$$\Lambda_{RCS} = \frac{|\text{RCS}_f(\text{object})|}{|\text{RCS}_f(\text{no object})|}. \quad (17)$$

The  $f$  subscript above denotes frequency averaging, which will be the focus of this case. The ACF and RCS are averaged from 150 to 450 MHz in 10-MHz steps. The angles chosen for this case are  $\theta_{s1} = 30^\circ$  and  $\theta_{s2} = -15^\circ$ . Examining the RCS alone at any single frequency is not useful in determining the presence of the target object because the response over angle shows only small fluctuations. The results are depicted in Figure 5, which compares  $\Lambda_{RCS}$  against  $\Lambda_{ACF}$ , where  $\Lambda_{ACF}$  is measured along and perpendicular to the memory line (intersecting at the peak). In this case, the presence of the object is difficult to determine solely with frequency averaging on the RCS because the difference does not fluctuate more than 1 dB. On the other hand, the ACF away from the memory line shows a correlation that is 16 dB greater when the object is present, and peaks at 3 dB elsewhere. The ACF along the memory line in this case is less effective, showing less change than the  $\Lambda_{RCS}$ . Note that the peak of the memory line occurs here in both cases at  $\theta_{s2} = -20^\circ$ , and at this point the ACF is least effective for target detection.

The effectiveness of examining the ACF variations away from the memory line is again demonstrated in Figure 6, where one of the scattered field directions is held constant at either  $\theta_{s1} = -30^\circ$  (specular direction) or  $\theta_{s1} = 30^\circ$  (back scattering). The ACF in the specular direction does little better than the RCS, but for  $\theta_{s1} = 30^\circ$ , two strong peak fluctuations of 9 and 10 dB are observed, as well as a third smaller peak of  $-4$  dB. These results suggest that a ground-penetrating radar setup could be designed to explore this effect by, for instance, employing two transmitting antennas at fixed angles (with one acting also as a receiver), and a third antenna acting only as a receiver that would scan over discrete angles or bands of angles.

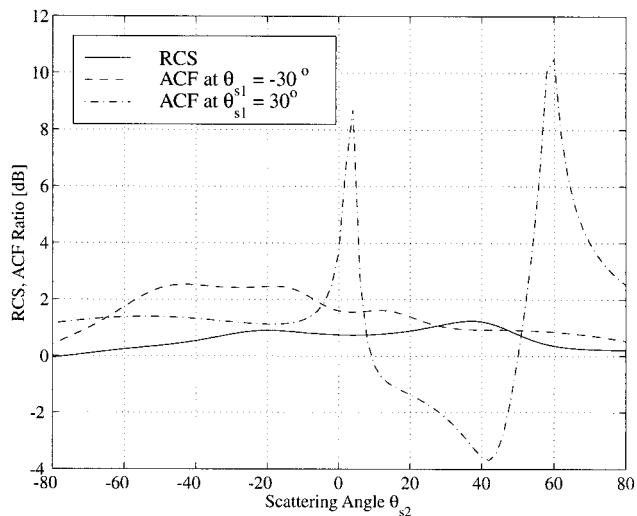


**Figure 6** Frequency-averaged RCS and ACF results, away from the memory line (specular and back scattering). The domain is  $3.2\lambda \times 3.2\lambda \times 1.6\lambda$

Finally, a larger domain simulation (larger illuminated volume) is examined. In this case, higher fluctuations in the ACF are expected to possibly cause larger fluctuations on  $\Lambda_{ACF}$  (because of the sinc-like behavior of the ACF). Figure 7 shows the  $\Lambda_{RCS}$  and  $\Lambda_{ACF}$  results for a random medium that is  $6.4\lambda \times 6.4\lambda \times 1.6\lambda$ .  $\Lambda_{RCS}$  in this case fluctuates between plus and minus 2 dB, as does  $\Lambda_{ACF}$  along the memory line. There are more interesting results for  $\Lambda_{ACF}$  perpendicular to the memory line, with larger fluctuations of 3 and  $-7$  dB. Moreover Figure 8, shows the  $\Lambda_{ACF}$  in the specular,  $\theta_{s1} = -30^\circ$ , and backscattering,  $\theta_{s1} = 30^\circ$ , directions fluctuating many times from 4 to 10 dB. Either scattering angle choice produces three or four large fluctuations, which would result in a useful criteria and better chance of object detection for a finite number of  $\theta_{s2}$  measurements. Note that these frequency-averaged results are obtained by considering a single particular realization of the random medium. Tests have been performed on different realizations and, although the details may vary, the same general behavior was observed.

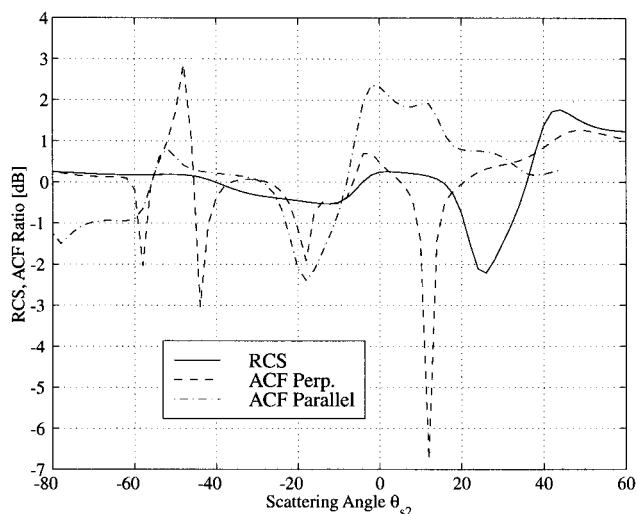


**Figure 7** Frequency-averaged RCS and ACF results, along and perpendicular to the memory line. The domain size is  $6.4\lambda \times 6.4\lambda \times 1.6\lambda$

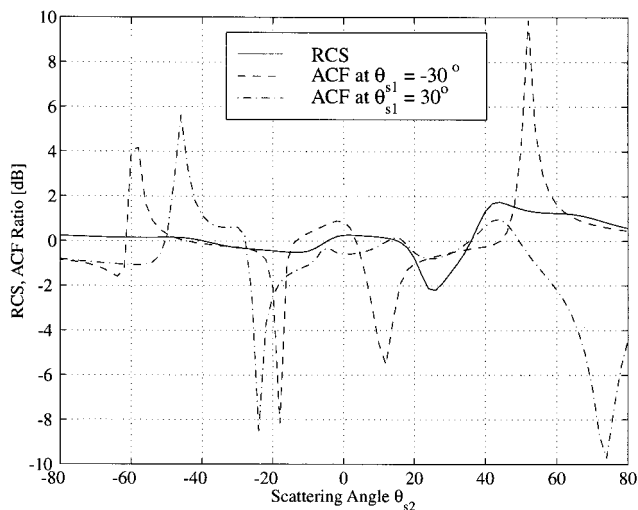


**Figure 8** Frequency-averaged RCS and ACF results, away from the memory line (specular and back scattering). The domain size is  $6.4\lambda \times 6.4\lambda \times 1.6\lambda$

## 6. CONCLUSION

Three-dimensional FDTD simulations have been employed to characterize the ACF of the scattering from targets in continuous random media. The memory effect of the ACF was clearly demonstrated through an average over random medium realizations. The effectiveness of the ACF in detecting a buried cylinder under frequency averaging was also demonstrated. When an object was placed in the medium, the ACF exhibited a much greater variation than the bistatic RCS, especially away from the memory line.

## REFERENCES

1. F.T. Ulaby, R.K. Moore, and A.K. Fung, *Microwave remote sensing: Active and passive*, Artech House, Boston, 1981.
2. M.Z.M. Jenu and D.H.O. Bebbington, Two-dimensional modelling of optical propagation in turbulent atmosphere, *Electron Lett* 29 (1993), 769–771.
3. K. O'Neill, R.F. Jr. Lussky, and K.D. Paulsen, Scattering from a metallic object embedded near the randomly rough surface of a lossy dielectric, *IEEE Trans Geosci Remote Sensing* GRS-34 (1996), 367–376.
4. T.J. Cui and W.C. Chew, Fast evaluation of Sommerfeld integrals for EM scattering and radiation by three-dimensional buried objects, *IEEE Trans Geosci Remote Sensing* GRS-37 (1999), 887–900.
5. K. Demarest, R. Plumb, and Z. Huang, FDTD modeling of scatterers in stratified media, *IEEE Trans Antennas Propagat* AP-43 (1995), 1164–1168.
6. D.A. Hill, Electromagnetic scattering by buried objects of low contrast, *IEEE Trans Geosci Remote Sensing* GRS-26 (1988), 195–203.
7. S. Vitebskiy, L. Carin, M.A. Ressler, and F.H. Le, Ultra-wideband, short-pulse ground-penetrating radar: Simulation and measurement, *IEEE Trans Geosci Remote Sensing* GRS-35 (1997), 762–772.
8. T. Dogaru and L. Carin, Time-domain sensing of targets buried under a rough air–ground interface, *IEEE Trans Antennas Propagat* AP-46 (1998), 360–372.
9. W.R. Scott and G.S. Smith, Measured electrical constitutive parameters of soil as functions of frequency and moisture content, *IEEE Trans Geosci Remote Sensing* GRS-30 (1992), 621–623.
10. J. Bourgeois, A complete three-dimensional electromagnetic simulation of ground-penetrating radars using the finite-difference time-domain method, Ph.D. thesis, Georgia Institute of Technology, 1997.
11. C.D. Moss, F.L. Teixeira, and J.A. Kong, Finite difference time domain simulation of scattering from objects in continuous random media, *IEEE Trans Geosci Remote Sensing*, to be published.

12. A. Taflov, *Computational electrodynamics: The finite-difference time-domain method*, Artech House, Boston, 1995.
13. C.D. Moss, Finite-difference time-domain simulation of electromagnetic scattering from objects under random media, M.S. thesis, Massachusetts Institute of Technology, 2000.
14. K. Demarest, Z. Huang, and R. Plumb, An FDTD near- to far-zone transformation for scatterers buried in stratified grounds, *IEEE Trans Antennas Propagat* AP-44 (1996), 1150–1157.
15. W.C. Chew and W.H. Weedon, A 3D perfectly matched medium from modified Maxwell's equations with stretched coordinates, *Microwave Opt Technol Lett* 7 (1994), 599–604.
16. M. Borgeaud, R.T. Shin, and J.A. Kong, Theoretical models for polarimetric radar clutter, *J Electromagnetic Waves Appl* 1 (1987), 73–89.
17. A.K. Fung and F.T. Ulaby, A scatter model for leafy vegetation, *IEEE Trans Geosci Electron* GE-16 (1978), 281–286.
18. S. Feng, C. Kane, P.A. Lee, and A.D. Stone, Correlations and fluctuations of coherent wave transmission through disordered media, *Phys Rev Lett* 61 (1988), 834–837.
19. G. Zhang and L. Tsang, Angular correlation function of wave scattering by a random rough surface and discrete scatterers and its application in the detection of a buried object, *Waves in random media*, 1997, Vol. 7, pp. 467–479.
20. L. Tsang, J.A. Kong, and K.H. Ding, *Scattering of electromagnetic waves: Theories and applications*, 1st ed., John Wiley & Sons, New York, 2000.
21. K.S. Yee, Numerical solution of initial boundary value problems involving Maxwell's equations in isotropic media, *IEEE Trans Antennas Propagat* AP-14 (1966), 302–307.
22. J.E. Hipp, Soil electromagnetic parameters as functions of frequency, soil density, and soil moisture, *Proc IEEE* 62 (1974), 98–103.
23. F.L. Teixeira, W.C. Chew, M. Straka, M.L. Oristaglio, and T. Wang, Finite-difference time-domain simulation of ground penetrating radar on dispersive, inhomogeneous, and conductive soils, *IEEE Trans Geosci Remote Sensing* GRS-36 (1998), 1928–1937.

© 2002 Wiley Periodicals, Inc.

## A DOUBLE FREQUENCY 180° LUMPED-ELEMENT HYBRID

Franco Giannini and Lucio Scucchia

Department of Electronic Engineering  
University of Roma Tor Vergata  
via Del Politecnico 1  
00133 Rome, Italy

Received 14 November 2001

**ABSTRACT:** In this letter design formulas for the development of an unusual 180° hybrid working at two distinct frequencies are provided. In particular, the design formulas of a lumped-element rat race are considered. © 2002 Wiley Periodicals, Inc. *Microwave Opt Technol Lett* 33: 247–251, 2002; Published online in Wiley InterScience (www.interscience.wiley.com). DOI 10.1002/mop.10288

**Key words:** lumped elements; pi networks; 180° hybrid; rat race; design formulas

## 1. INTRODUCTION

At frequencies below 20 GHz the conventional transmission-line rat races occupy a large surface and create dimensional problems in MMICs, so generally at these frequencies rat races are realized with lumped elements.

In order to design a rat race with lumped elements, the transmission-line segments of a conventional rat race are replaced with